Science Advances
AAAS

advances.sciencemag.org/cgi/content/full/4/10/eaar5278/DC1

Supplementary Materials for

Observation of long-range dipole-dipole interactions in hyperbolic metamaterials

Ward D. Newman, Cristian L. Cortes, Amir Afshar, Ken Cadien, Al Meldrum, Robert Fedosejevs, Zubin Jacob*

*Corresponding author. Email: zjacob@purdue.edu

Published 5 October 2018, *Sci. Adv.* **4**, eaar5278 (2018)
DOI: 10.1126/sciadv.aar5278

This PDF file includes:

Section S1. Theory of resonant dipole-dipole interactions in hyperbolic media

1 RDDI Fields

Here, we provide the formal relation between the resonant dipole-dipole interaction and the classical dyadic Green function in a hyperbolic medium. Following [11], the resonant dipole-dipole interaction for two neutral atoms in an arbitrary nanophotonic environment is

$$V_{dd} = -\frac{\omega^2}{\epsilon_o c^2}\mathbf{d}_B \cdot \mathbf{G}(\mathbf{r}_B, \mathbf{r}_A; \omega) \cdot \mathbf{d}_A \tag{1}$$

for two two-level atoms initially prepared in the symmetric or anti-symmetric state ($|i\rangle = \frac{1}{\sqrt{2}}(|a'\rangle|b\rangle \pm |a\rangle|b'\rangle) \otimes |\{0\}\rangle$) [44]. Here, $\mathbf{d}_{A(B)}$ is the purely electronic transition dipole matrix element between the electronic ground $|a\rangle$ ($|b\rangle$) and excited state $|a'\rangle$ ($|b'\rangle$) of atom A(B).

For the case of two molecules, the total transition matrix element is given by $d_{aa'(bb')} = \mathbf{d}_{A(B)} v_{aa'(bb')}$ in the Born-Oppenheimer approximation. $v_{aa'(bb')}$ corresponds to the overlap integral between the vibrational states of each respective molecule. When molecule A is initially prepared in its excited electronic state and molecule B is in its electronic ground state ($|i\rangle = |a'\rangle|b\rangle \otimes |\{0\}\rangle$ then, through Fermi's Golden rule, the total Förster Resonance Energy Transfer (FRET) rate from molecule A to molecule B is given by

$$\Gamma_{ET} = \frac{2\pi}{\hbar^2}\int d\omega\, |V_{dd}(\omega)|^2 \sigma_A(\omega)\sigma_B(\omega) \tag{2}$$

where $\sigma_A(\omega)$ and $\sigma_B(\omega)$ are proportional to the emission spectrum and absorption spectrum of molecule A and B respectively

$$\sigma_A(\omega) = \sum_{a,a'} p'_a |v_{aa'}|^2 \delta(\omega_{a'a} - \omega) \tag{3}$$

and

$$\sigma_B(\omega) = \sum_{b,b'} p_b |v_{b'b}|^2 \delta(\omega_{b'b} - \omega) \tag{4}$$

where p_i is the occupation probability of state $|i\rangle$. To obtain equation (1) in the main text, we utilize the dyadic Green function for a dipole in an uniaxial medium with optic axis $\hat{\mathbf{c}}$. The dyadic Green's Tensor is given by

$$\begin{aligned}\mathbf{G}(\mathbf{r}, \mathbf{r}'; \omega) = \frac{1}{4\pi\sqrt{\epsilon_x}}\Bigg\{ &\frac{e^{ik_o r_e}}{r_e}\Bigg[\left(\frac{k_o^2 r_e^2 + ik_o r_e - 1}{k_o^2 r_e^2}\right)\epsilon_x\epsilon_z\boldsymbol{\epsilon}^{-1} \\ &- \left(\frac{k_o^2 r_e^2 + 3ik_o r_e - 3}{k_o^2 r_e^2}\right)\frac{\epsilon_x^2\epsilon_z^2(\boldsymbol{\epsilon}^{-1}\cdot\mathbf{r})(\boldsymbol{\epsilon}^{-1}\cdot\mathbf{r})}{r_e^2} \\ &+ \left(\frac{\epsilon_x e^{ik_o r_o}}{r_o} - \frac{\epsilon_z e^{ik_o r_e}}{r_e}\right)\frac{(\mathbf{r}\times\hat{\mathbf{c}})(\mathbf{r}\times\hat{\mathbf{c}})}{(\mathbf{r}\times\hat{\mathbf{c}})^2} + \frac{e^{ik_o r_o} - e^{ik_o r_e}}{ik_o(\mathbf{r}\times\hat{\mathbf{c}})^2}\left[\mathbf{I} - \hat{\mathbf{c}}\hat{\mathbf{c}} - 2\frac{(\mathbf{r}\times\hat{\mathbf{c}})(\mathbf{r}\times\hat{\mathbf{c}})}{(\mathbf{r}\times\hat{\mathbf{c}})^2}\right]\Bigg\}\end{aligned} \tag{5}$$

where $r_e = rN(\theta) = r\sqrt{\epsilon_z \sin^2\theta + \epsilon_x \cos^2\theta}$ and $r_o = r\sqrt{\epsilon_x}$. The Super-Coulombic dipole-dipole interaction occurs when two molecules are positioned such that the radius vector separating the two is parallel to the hyperbolic metamaterial's resonance cone whose half opening angle is $\theta_R = \tan^{-1}\sqrt{-\epsilon_x/\epsilon_z}$. Near this resonance angle, the Green tensor is approximately

$$\mathbf{G}(\mathbf{r}, \mathbf{r}'; \omega) \approx \frac{e^{ik_o r_e}}{4\pi\epsilon_o\sqrt{\epsilon_x} r_e^3}\left[(1 - ik_o r_e)\boldsymbol{\kappa}_{nf} - k_o^2 r_e^2 \boldsymbol{\kappa}_{ff}\right] \tag{6}$$

where we have defined the material dependent near-field and far-field dipole orientation matrix factors $\boldsymbol{\kappa}_{nf} = \epsilon_x\epsilon_z(\boldsymbol{\epsilon}^{-1} - 3(\boldsymbol{\epsilon}^{-1}\cdot\mathbf{r})(\boldsymbol{\epsilon}^{-1}\cdot\mathbf{r})/(\mathbf{r}\cdot\boldsymbol{\epsilon}^{-1}\cdot\mathbf{r}))$ and $\boldsymbol{\kappa}_{ff} = \epsilon_x\epsilon_z(\boldsymbol{\epsilon}^{-1} - (\boldsymbol{\epsilon}^{-1}\cdot\mathbf{r})(\boldsymbol{\epsilon}^{-1}\cdot\mathbf{r})/(\mathbf{r}\cdot\boldsymbol{\epsilon}^{-1}\cdot\mathbf{r}))$ respectively. To obtain equation (1) in the main text, we retain highest order diverging terms proportional to r_e^{-3} near $\theta \to \theta_R$. The experimental signature of FRET is the reduction in the excited state lifetime

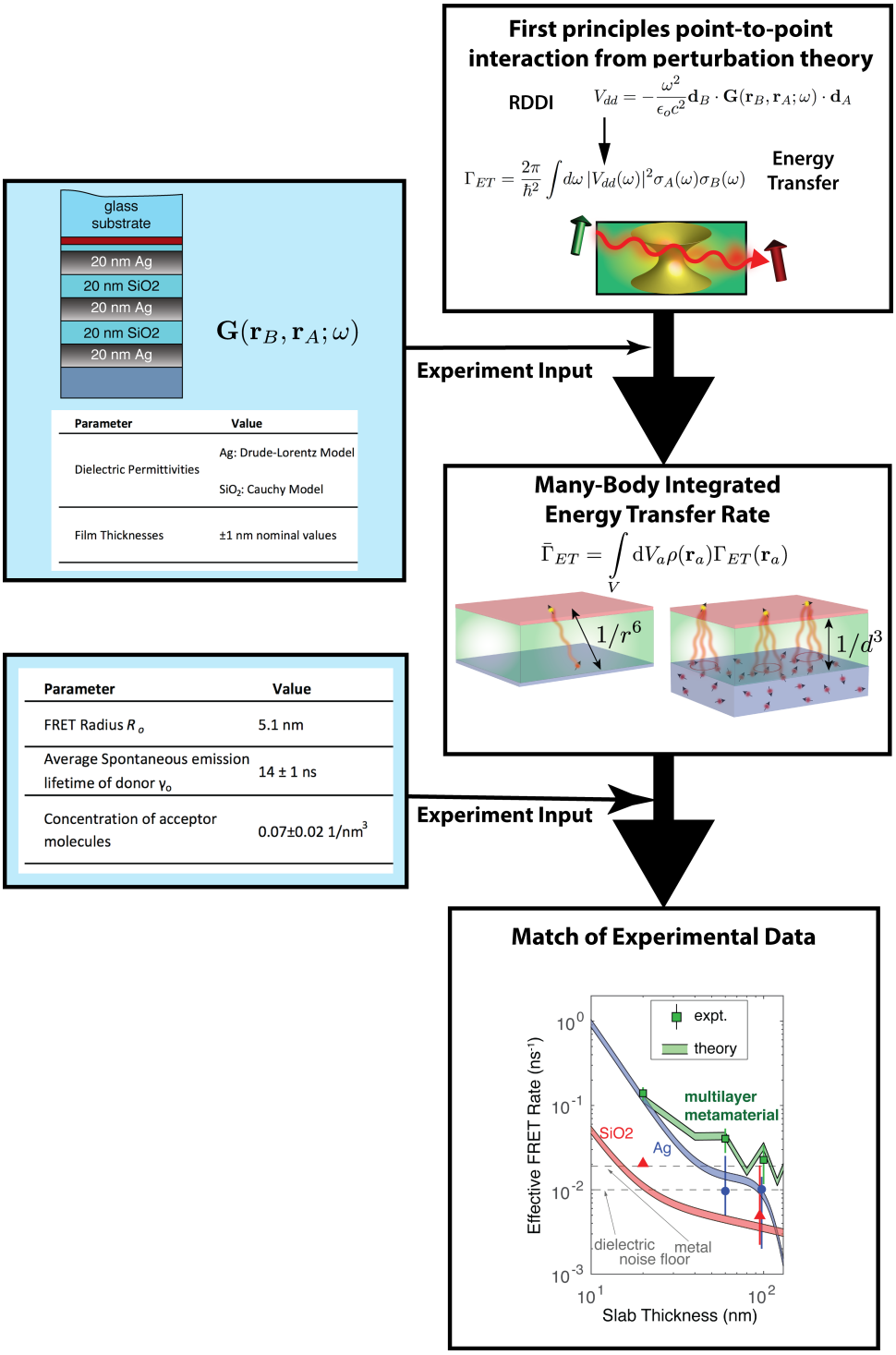

Fig. S1. Flowchart of comparison between experiment and theory. The flow chart is shown describing our first principles method for going from point-to-point super-Coulombic dipole-dipole interactions, to the many body ensemble dipole-dipole interactions we observe in experiment. Experimental parameters, extracted from independent experiments and measurements, are inserted into the model process flow at various stages of the procedure as shown in the blue shaded boxes. Dielectric permittivities and geometric size parameters are used for the analytic simulation of the electrodynamic response of multilayer structures ($\mathbf{G}$), which in turn is used to compute the realistic Super-Coulombic interaction potential. The FRET radius, donor spontaneous emission lifetime and acceptor concentration profile are used in the ensemble averaging of the point-to-point interactions. We emphasize that we do not use fitting parameters or free variables to compare theory and experiment.

of atom A which is sensitive to the presence of atom B in the near-field. When interacting through a hyperbolic medium, a fundamental difference in the lifetime is expected due to the Super-Coulombic effect. Note this equation together with equation (2) forms the basis of Super-Coulombic FRET in hyperbolic metamaterials.

Note that in the ideal low-loss effective medium limit, the point dipole approximation breaks down for extremely closely spaced quantum emitters. In our experiment and numerical simulations of the practical metamaterial, the point dipole approximation is valid since the metamaterial unit cell sizes and interaction length scales are larger than the molecule sizes. The local density of states inside a lossy medium diverges in the local macroscopic electrodynamic theory. For the case of hyperbolic media, there exists a divergence even in the low-loss effective medium limit due to the unbounded nature of the hyperboloidal k-surface. In our theory of super-Coulombic resonant dipole-dipole interactions in lossy hyperbolic media, these divergences are curtailed by the cut-off length scale due to the finite distance between interacting quantum emitters.Our results on long-range energy transfer also directly imply that the non-equilibrium van der Waals interaction (thermal fluctuation driven forces) between embedded macroscopic scatterers in a hyperbolic medium would be enhanced and long-range.

Relation to experiment. In order to relate the theory to the main experiment described in the manuscript, we use the famous Forster formula

$$\frac{\Gamma_{ET}}{\gamma_o} = 18\pi \int_0^\infty f_d(\omega)\sigma_a(\omega)|\mathbf{n}_a \cdot \mathbf{G}(\mathbf{r}_A, \mathbf{r}_D; \omega) \cdot \mathbf{n}_d|^2 d\omega \tag{7}$$

expressed in terms of the normalized emission spectrum $f_d(\omega)$ of the donor, as well as the absorption cross-section $\sigma_a(\omega)$ of the acceptor molecule determined through photoluminescence and transmission measurements. Here, γ_o is the donor decay rate measured in a homogeneous environment with $\mathbf{n}_a$ and $\mathbf{n}_d$ representing the unit orientation vectors for each dipole. This formula is more easily related to measured quantities in experiments, allowing us to provide a direct comparison between theory and experiment.

The emission and absorption spectrum of Alq3 and R6G are shown in figure S6. Generally, all environmental information is contained in the Green function. In free-space this quantity is frequency-independent in the near-field limit ($kr \ll 1$), therefore, one may remove the Green function contribution from the spectral integral resulting in the conventional definition of the FRET radius

$$R_o^6 = QY \frac{9c^4\kappa^2}{8\pi} \int_0^\infty \frac{f_d(\omega)\sigma_a(\omega)}{n^4\omega^4} d\omega \tag{8}$$

For general nanophotonic environments, this definition of the FRET radius is not possible due to the general spectral dependence of the Green function. The transmission data for extraordinarily polarized waves [1] In the emission-absorption overlap region, the transmittance of our multilayered structure changes very slowly as a function of wavelength indicating that the permittivity values also change slowly in the overlap region. This suggests we can remove the Green function dependence from the spectral integral and approximate the FRET rate as

$$\frac{\Gamma_{ET}}{\gamma_o} = 16\pi^2 k^4 R_o^6 \, |\mathbf{n}_a \cdot \mathbf{G}(\mathbf{r}_A, \mathbf{r}_D; \omega_{da}) \cdot \mathbf{n}_d|^2 \tag{9}$$

where the FRET radius is equivalent to the conventional definition. The Green function is evaluated at the peak of the emission-absorption spectrum overlap.

2 Point-to-Point Super-Coulombic FRET across a hyperbolic metamaterial

We utilize the full form of the Green dyadic in multilayered geometries. This calculation provides the RDDI strength as a function of acceptor position (fixed $\mathbf{r}$ with variable $\mathbf{r}'$), showing the enhancement and directionality [12] of intermolecular interaction strengths between donor and acceptor molecules mediated by hyperbolic modes. The HMM allows a single donor to interact with several acceptors due to the multiple reflections of the directional hyperbolic polaritons along the asymptotes.

[1] Extraordinary waves are propagating waves in a uniaxial media with electric field components both along and perpendicular to the optic axis which is the z-axis for our convention. They probe two different components of the uniaxial dielectric tensor. Ordinary waves, on the other hand, have their electric fields polarized normal to the optic axis (in the x-y plane) and probe only one component of the uniaxial dielectric tensor giving electromagnetic responses similar to an isotropic medium.

3 Many-dipole interactions and unique scaling laws with photoluminescence studies

3.1 Analytical Approach: *The Thermodynamic Limit*

To confirm the nature of the Super-Coulombic dipole-dipole interaction over large intermolecular distances, we performed time-resolved ensemble measurements of the donor fluorescence intensity. In the following, we provide a simple derivation showing how the integrated (many-body) energy transfer rate emerges naturally from donor photoluminescence studies.

In general, the fluorescence intensity decay trace of a donor surrounded by N_a acceptor molecules depends on the probability of the energy transfer from the donor to each of the acceptors. For a given configuration specified by the donor position $\mathbf{r}_D$, and acceptor positions $\mathbf{r}_{Aj}$, the total donor decay rate γ_D is given by $\gamma_D = \gamma_o + \sum_i^{N_a} \Gamma_{ET}(\mathbf{r}_{Ai}, \mathbf{r}_D)$, where γ_o is the spontaneous emission rate of the donor in the absence of acceptor molecules. The total donor intensity decay trace is given by [44]

$$\begin{aligned} I_D(t) &\sim e^{-\gamma_o t} \int d\mathbf{r}_{A1}\, \rho(\mathbf{r}_{A1}) \int d\mathbf{r}_{A2}\, \rho(\mathbf{r}_{A2}) \cdots \int d\mathbf{r}_{AN_a}\, \rho(\mathbf{r}_{AN_a}) e^{-t\sum_i \Gamma_{ETi}(\mathbf{r}_{Ai}, \mathbf{r}_D)} \\ &\sim e^{-\gamma_o t} \left[\int d\mathbf{r}_A\, \rho(\mathbf{r}_A) e^{-t\Gamma_{ET}(\mathbf{r}_A, \mathbf{r}_D)} \right]^{N_a} \end{aligned} \tag{10}$$

In the limit of small point-to-point energy transfer rates $t\Gamma_{ET} \ll 1$, an assumption that is generally valid for large separation distances between donors and acceptors, we may expand the exponential to give the final result

$$I_D(t) \approx e^{-\gamma_o t} \left[\int d\mathbf{r}_A\, \rho(\mathbf{r}_A)(1 - t\Gamma_{ET}(\mathbf{r}_A, \mathbf{r}_D)) \right]^{N_a} \tag{11}$$

$$\sim e^{-\gamma_o t} \exp\left[-c_A \int d\mathbf{r}_A \Gamma_{ET}(\mathbf{r}_D, \mathbf{r}_A) t \right] \tag{12}$$

for a uniform acceptor density $\rho(\mathbf{r}_a)$ in the thermodynamic limit ($N_a \to \infty, V_a \to \infty, N_a/V_a \to$ const). The result shows the spontaneous emission rate γ_o of a donor will be modified by an integrated energy transfer rate over many acceptor dipoles. In the following, we show how the integrated energy transfer rate displays unique spatial scaling laws owing to the Coulombic power law dependence $\Gamma_{ET} \sim r^{-6}$.

4 Many-body integrated energy transfer rate

Application to multi-layered nanophotonic environments

We now show how the FRET rate changes when there is a large distribution of acceptors. Using (9), the general result for the integrated energy transfer is obtained though evaluation of the integral

$$\bar{\Gamma}_{ET} = \gamma_o 16\pi^2 k^4 R_o^6 c_a \int d\mathbf{r}_a |\mathbf{n}_a \cdot \mathbf{G}(\mathbf{r}_A, \mathbf{r}_D; \omega_{da}) \cdot \mathbf{n}_d|^2 \tag{13}$$

valid for arbitrary nanophotonic environments.

For multi-layered systems with cylindrical symmetry, the dyadic elements of the Green function can be written in the form $G_{ij} \sim \int dk_\rho\, f_{ij}(k_\rho) J_n(k_\rho \rho) \cos(n\theta)$ or $G_{ij} \sim \int dk_\rho\, f_{ij}(k_\rho) J_n(k_\rho \rho) \sin(n\theta)$, where $f_{ij}(k_\rho)$ is a function containing the reflection or transmission coefficients of the environment, while $J_n(k_\rho)$ is the cylindrical Bessel function of order n. In cylindrical coordinates, the integral over the acceptor surface area yields the following types of integrals

$$\int_0^{2\pi} d\theta \int_0^\infty \rho\, d\rho\, |\mathbf{n}_a \cdot \mathbf{G}(\mathbf{r}_A, \mathbf{r}_D) \cdot \mathbf{n}_d|^2 \sim \begin{cases} \int_0^{2\pi} \cos(n\theta)\cos(m\theta) d\theta \int_0^\infty \rho J_n(k_\rho \rho) J_m(k'_\rho \rho) d\rho \\ \int_0^{2\pi} \sin(n\theta)\sin(m\theta) d\theta \int_0^\infty \rho J_n(k_\rho \rho) J_m(k'_\rho \rho) d\rho \\ \int_0^{2\pi} \cos(n\theta)\sin(m\theta) d\theta \int_0^\infty \rho J_n(k_\rho \rho) J_m(k'_\rho \rho) d\rho \end{cases}$$

The orthogonality relations of trigonometric functions, together with the closure relation of the Bessel function ensures a complete evaluation of the surface integral for any component of the Green function. In the following we provide an exact expression for the spatially integrated transmitted Green function.

In the experiment, a linearly polarized laser excites donor dipoles lying parallel to the interface, therefore we only provide here the Green function components related to parallel (x-oriented) donor dipole

$$G_{xx}(\mathbf{r}) = \frac{i}{8\pi k_1^2}\int dk_\rho \frac{k_\rho}{k_z} e^{ik_z(z_a+z_d)}\left[t_{ss}k_1^2 J_+^c + k_z^2 J_-^c t_{pp}\right] \tag{14}$$

$$G_{yx}(\mathbf{r}) = \frac{i}{8\pi k_1^2}\int dk_\rho \frac{k_\rho}{k_z} e^{ik_z(z_a+z_d)}\left[k_1^2 t_{ss} - k_z^2 t_{pp}\right] J_2(k_\rho\rho)\sin 2\theta \tag{15}$$

$$G_{xz}(\mathbf{r}) = \frac{i}{8\pi k_1^2}\int dk_\rho k_\rho^2 e^{ik_z(z_a+z_d)}\left[2it_{pp}J_1(k_\rho\rho)\cos(\theta)\right] \tag{16}$$

where we have used the shorthand notation for the cylindrical bessel functions $J_\pm = J_o(k_\rho\rho) \pm J_2(k_\rho\rho)\cos 2\theta$. The final result of the integrated energy transfer rate for a two-dimensional sheet of acceptor is

$$\int_0^{2\pi} d\theta \int_0^\infty \rho\, d\rho\, |G_{xx}|^2 = \frac{\pi}{|8\pi k_1^2|^2}\int dk_\rho \frac{k_\rho}{|k_z|^2} e^{i(k_z-k_z^*)(z_a+z_d)}\left[3|t_{ss}k_1^2|^2 + 3|t_{pp}k_z^2|^2 + t_{pp}t_{ss}^* k_z^2 k_1^2 + t_{pp}^* t_{ss} k_z^{2*} k_1^2\right] \tag{17}$$

$$\int_0^{2\pi} d\theta \int_0^\infty \rho\, d\rho\, |G_{zx}|^2 = \frac{4\pi}{(8\pi k_1^2)^2}\int dk_\rho k_\rho^3 e^{i(k_z-k_z^*)(z_a+z_d)}|t_{pp}|^2 \tag{18}$$

$$\int_0^{2\pi} d\theta \int_0^\infty \rho\, d\rho\, |G_{yx}|^2 = \frac{\pi}{|8\pi k_1^2|^2}\int dk_\rho \frac{k_\rho}{|k_z|^2} e^{i(k_z-k_z^*)(z_a+z_d)}|t_{ss}k_1^2 - t_{pp}k_z^2|^2 \tag{19}$$

To take into account the finite size of the acceptor slab thickness, we evaluate the following integral

$$\int_0^{t_a} dz_a\, e^{-2\mathrm{Im}[k_z]z_a} = \frac{1-e^{-2\mathrm{Im}[k_z]t_a}}{2\mathrm{Im}[k_z]} \tag{20}$$

and use the substitution $e^{i(k_z-k_z^*)(z_d+z_a)} \to \frac{1-e^{-2\mathrm{Im}[k_z]t_a}}{2\mathrm{Im}[k_z]}$ in all of the previous equations.

Comparison to well known energy transfer power laws

The energy transfer between a donor and a sheet of acceptors of concentration c_A separated by a distance d, or equivalently a sheet-to-sheet interaction, is given by

$$\int_0^\infty \Gamma_{ET}\, c_A \rho d\rho = \int_0^\infty \frac{c_A\gamma_o\rho d\rho}{(d^2+\rho^2)^3} = \frac{R_o^6}{4d^4}c_A\gamma_o \tag{21}$$

assuming near-field (Coulombic) coupling, $\Gamma_{ET} = (R_o/r)^6\gamma_o$. Integrating over acceptor slab thickness, as before, results in the d^{-3} Coulombic scaling dependence. The result shown in figure S2 compares the 2D and 3D scaling arising from a finite-slab (20 nm) of acceptors and 2D sheet of acceptors. Note that the result in the figure is calculated with the integral expressions in k-space, clearly reproducing the limiting power law behavior derived in this sub-section.

Spectral dependence of integrated energy transfer. We now discuss spectral dependence of the many-body energy transfer rate. As mentioned earlier, the total energy transfer rate involves spectral integration as well as spatial integration of the acceptor volume. For our calculations, we assumed to energy transfer rate varies slowly as a function of wavelength; the result shown in figure 4 confirms the slowly-varying spectral dependence in the near-field of the metamaterial. We use the permittivity parameters extracted experimentally, and plot the integrated energy transfer rate across a 100 nm hyperbolic medium (using the effective medium model), 100 nm silver film, and 100 nm SiO_2 layer. The results are shown for different dipole orientations, clearly demonstrating that the spectrum changes very slowly in the donor-acceptor overlap region between 500 and 600 nm.

Wavevector-resolved energy transfer. Using the expressions derived above, we now show the resolved energy transfer rate in terms of its k-space spatial frequency modes. Note that these results are analogous to the k-resolved local density of states used in nanophotonics, however, we emphasize that this is a non-local quantity applying to the integrated energy transfer rate. In figure S2, we show

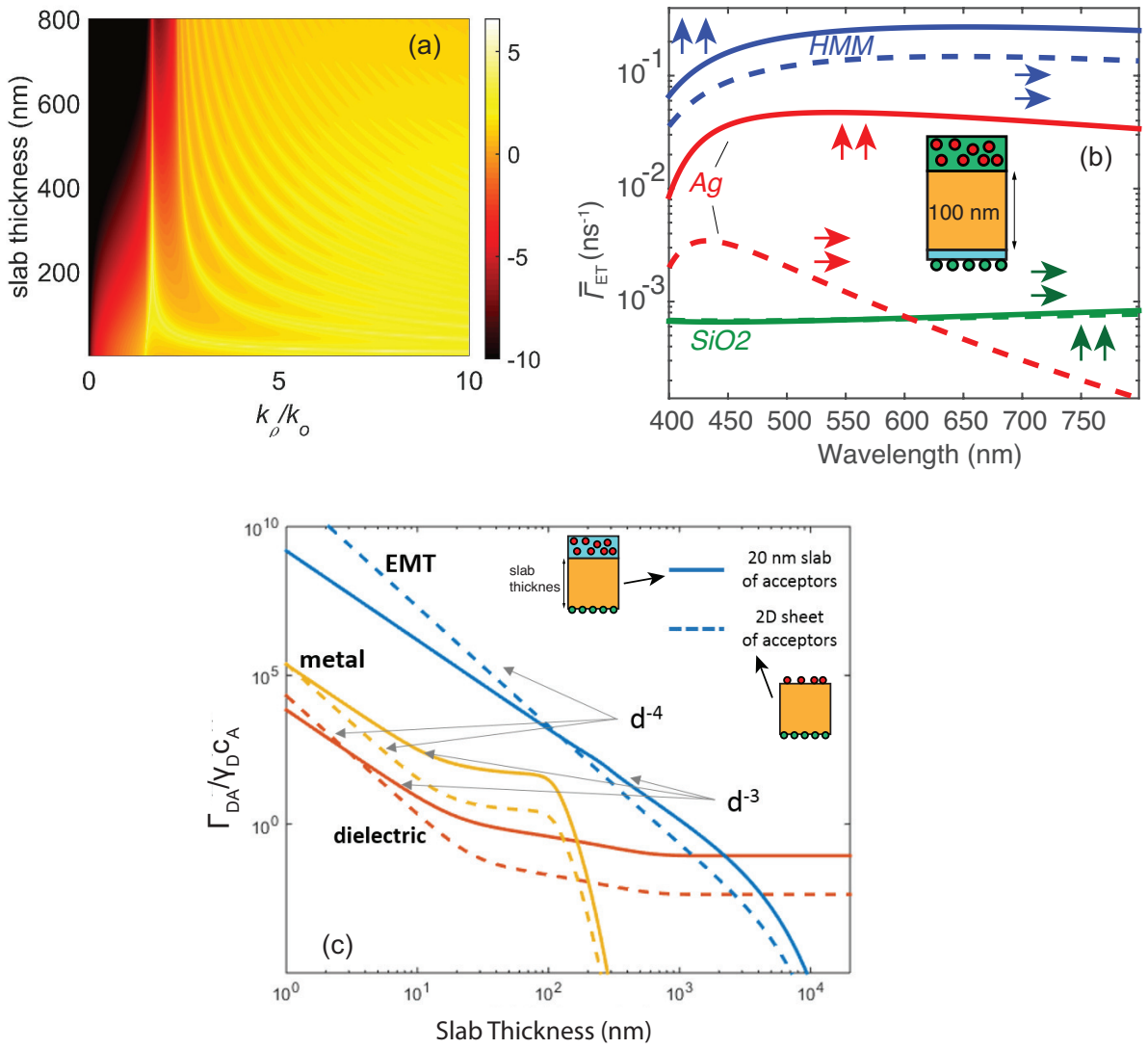

Fig. S2. (a) Long-distance sheet-to-sheet super-Coulombic dipole-dipole interactions in a hyperbolic medium.

the origin of the extended Super-Coulombic scaling law as a result of the high-k hyperbolic polariton modes allowed in a hyperbolic medium. Note that for large slab thicknesses, the near-field scaling is curtailed by dissipative losses resulting in damped high-k modes. Interestingly, the high-k spatial frequency modes retain a longitudinal character even for large separation ditances, thereby resulting in the novel Super-Coulombic power law.

In figure S2, we separate the radiative $[0, \sqrt{\epsilon_1}\omega/c]$ and non-radiative contributions $[\sqrt{\epsilon_1}\omega/c, \infty]$ contributions to the integrated energy transfer rate. This is achieved using the k-resolved spatial frequency integrals derived above. Note that the practical multi-layer structure with 40 nm unit-cell size agrees with ideal effective medium model, whereby the total contribution to the energy transfer rate originates from the non-radiative modes. Of particular importance, this occurs both in the near-field ($kr \ll 1$) and ($kr \gg 1$) far-field separation limits. The results show a stark contrast to the dielectric and metal cases where there is a transition to radiative-dominated energy transfer above 30 nm for the dielectric case, and 650 nm for the metal case. Note that the energy transfer for the metal case becomes vanishingly small after 100 nm.

Net role of material absorption. To understand the role of material absorption on the integrated energy transfer rate through a slab, we now study the FRET rate as a function of slab thickness for various material absorption parameters. Material absorption is denoted by the imaginary component of the permittivity (ϵ''). As shown in figure S2, a low-loss hyperbolic medium $\epsilon'' \ll 1$ will exhibit the Coulombic power law scaling d^{-3} for an extended spatial range $> 10\,\mu$m. Ultimately, the near-field Coulombic law is curtailed by losses and has a finite spatial range of $\xi^{-1} = \omega/c\sqrt{(\epsilon_z''|\epsilon_x'| + \epsilon_z''|\epsilon_x'|) \,/\, (|\epsilon_x'| + |\epsilon_z'|)}$. Note that this expression serves as an important figure of merit that can be used to compare hyperbolic media platforms for energy transfer.

Figure S2 describes the scaling law of energy transfer between a 2D sheet of donors and a 2D sheet of acceptors absorbed to opposite surface of the HMM is shown versus the sheet-to-sheet separation by a slab. We observe the persistence of the near-field Coulombic scaling law (d^{-4}) up to 5-10 μm, 500$\times$ the conventional near-field of 5-10 nm. Note the subtle difference from the sheet-to-slab interaction scaling of (d^{-3}). The near-field scaling is eventually curtailed by dissipative losses at large distances. The top left figure in figure S2 shows this extension of the Coulombic near-field originates from the high spatial frequency bulk hyperbolic polaritons that propagate in the metamaterial. This is evident from the figure on the right which shows that waves with large wavevectors (momentum) normally evanescent in vacuum contribute strongly to the integrated Forster resonance energy transfer rate (color bar is normalized to the spontaneous emission rate in SiO_2). These high-spatial frequency modes retain a longitudinal character even at large propagation distances, a fundamental requirement for near-field Coulombic interactions. A quantitative comparison is shown of the total ensemble energy transfer (normalized by donor spontaneous emission lifetime and acceptor concentration) power law behavior for dielectric, metal, and ideal hyperbolic medium. The donors are assumed to be absorbed to the slab surface. This helps recover the scaling law for the case of embedded emitters. The operation wavelength, here is $\lambda = 520$ nm. Shown are the results for infinitely thin sheet of acceptors labeled as the 2D case, as well as for the finite-sized 20 nm slab of acceptors (as seen in experiment). We clearly see distinct power laws for short donor-acceptor separation distances corresponding to d^{-3} and d^{-4} scaling dependence. This subtle difference arises for a slab of acceptors or a 2D sheet of acceptors and is essential to account for in the comparison between theory and experiment. We emphasize that both these power laws fundamentally arise from the near-field Coulombic r^{-6} point-to-point interaction. The near-field is extended in the case of the EMT metamaterial over 1.5 orders of magnitude relative to conventional materials. The near-field scaling law in the EMT is eventually curtailed at total metamaterial thickness ξ, defined by material loss as $\xi^{-1} = \omega/c\sqrt{(\epsilon_z''|\epsilon_x'| + \epsilon_z''|\epsilon_x'|) \,/\, (|\epsilon_x'| + |\epsilon_z'|)}$. (c) The long range Super-Coulombic energy transfer is broadband and is present everywhere hyperbolic dispersion exists ($>$ 370 nm in our experiment). The effective energy transfer rate across 100 nm slabs of HMM (blue), Ag (red) and SiO_2 (green) is shown for different ensembles of dipole orientations ($\uparrow\uparrow$ refers to doth donor and acceptor dipoles vertical (perpendicular to the thin film interface), and $\rightarrow\rightarrow$ refers to both donors and acceptors horizontal). The donors are assumed to be 3.5 nm below the slab, as in experiment. The super-Coulombic enhancement of energy transfer across the HMM is considerably less sensitive to relative dipole-dipole orientations than the metallic case.

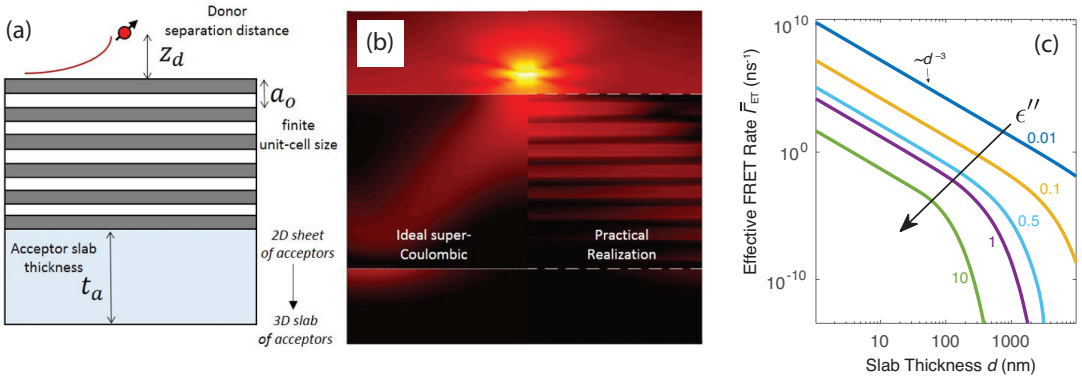

Fig. S3. (a,b) Interplay of length scales causing deviations from EMT. We note that our experimental results match the theoretical predictions of super-Coulombic scaling. Deviations from EMT occur due to the finite unit cell size as well as the finite separation distance of the donor emitters from the metamaterial. (right) The ideal super-Coulombic interaction at the resonance angle due to a dipolar emitter is well captured by the practical multi-layer realization. (c) A quantitative comparison is shown of the total sheet (donors) to slab (acceptors) ensemble energy transfer across a EMT HMM slab, as a function of total metamaterial thickness and material loss ϵ''. The near-field scaling law persists indefinitely until it is eventually curtailed at a total metamaterial thickness ξ, defined by material loss as $\xi^{-1} = \omega/c\sqrt{(\epsilon_z''|\epsilon_x'| + \epsilon_z''|\epsilon_x'|) \,/\, (|\epsilon_x'| + |\epsilon_z'|)}$. Here we assume isotropic loss: $\epsilon_x'' = \epsilon_z'' = \epsilon''$.

Section S2. Experimental verification of super-Coulombic dipole-dipole interactions

1 Experimental Determination of Average Decay Rates of Donors

In this section, we describe how we extract the effective FRET rate across metamaterials.

We utlize time-correlated single photon counting (TCSPC) to measure our fluorescence decay traces. Microscopically, the fluorescence decay $I(t)$ that we detect with TCSPC originates from a discrete number of emitters. Each emitter can emit at most one photon per laser pump pulse. This is a good assumption since the excited state lifetimes of the emitters (100 ps - 200 ns) is much longer than the duration of the laser pump pulse in our experiments (25-40 fs). Therefore, if the laser pump pulse has triggered an emitter to make a transition to its excited state, there is a $> 99.98\%$ probability the emitter is still in the excited state by the time the laser pump pulse has propagated away.

In the continuum limit of arbitrarily long acquisition times (many many observed detector clicks), the i^{th} emitter, will emit a decaying single exponential after the pump laser has arrived (and gone) so that our detected signal from this i^{th} single emitter takes the form

$$I_i(t) = u(t - t_o)\mathrm{e}^{-\gamma_i(t-to)} \tag{22}$$

where $u(t)$ is the unit step heaviside function, γ_i is the fluorescence decay rate of the i^{th} emitter, and t_o is the arrival time of the laser pump pulse at the emitter [19]. In these nanoscale geometries t_o can be taken as the same constant for all emitters since the transit time of the pulse through the sample (≈ 1 fs) is much shorter than our instrument response time of the TCSPC apparatus ($\approx$35 ps).

In experiment, we simultaneously measure the fluorescence decay trace of many donors ($> 10,000$) at once, each of which will emit a unique decaying single exponential with decay rate γ_i. In this limit of many emitters, the fluorescence decay trace $I(t)$ in general will be multi-exponential and can be approximated as a Laplace Transform of a continuous distribution of decay rates, that is an integral of a distribution of decaying exponentials

$$I(t) = \int_0^\infty \mathrm{d}\gamma\ A(\gamma)u(t)\mathrm{e}^{-\gamma t} \tag{23}$$

where $A(\gamma)$ is the distribution of *decay rates* present in the signal $I(t)$ for $t > 0$. We have now set t_o or simplicity without a loss of generality.

If the fluorescence decay trace $I(t)$ is normalized such that $I(t = 0^+) \equiv 1$, we necessarily apply the normalization condition

$$1 \equiv \int_0^\infty \mathrm{d}\gamma\ A(\gamma) \tag{24}$$

on the distribution of decay rates. With this normalization, the integral over all times of the decay trace yields

$$\int_{-\infty}^{\infty} \mathrm{d}t\ I(t) = \int_{-\infty}^{\infty} \mathrm{d}t \int_0^\infty \mathrm{d}\gamma\ A(\gamma)u(t)\mathrm{e}^{-\gamma t} \tag{25}$$

$$= \int_0^\infty \mathrm{d}\gamma\ \frac{1}{\gamma}A(\gamma) \tag{26}$$

We now note that the Harmonic mean of a decay rate distribution is rigorously defined as

$$\bar{\gamma} = \left(\frac{\int_0^\infty \mathrm{d}\gamma\ \frac{1}{\gamma}A(\gamma)}{\int_0^\infty \mathrm{d}\gamma\ A(\gamma)} \right) \tag{27}$$

Since we have $1 \equiv \int_0^\infty \mathrm{d}\gamma\ A(\gamma)$, then the integral

$$\int_0^\infty \mathrm{d}t\ I(t) = \bar{\gamma}^{-1} \tag{28}$$

That is, by normalizing our measured decay traces I(t=0) = 1, we can estimate our average donor decay rates by integrating the observed decay trace and performing a single division.

To quantify the additional decay pathway of the donor molecules with the acceptor molecules present on the opposite of the metamaterial, we subtract the effective decay rate (eq. 28 above) of the donor alone measurements with that of the donor with acceptors

$$\Gamma_{\mathrm{ET}} = \bar{\gamma}_{\mathrm{DA}} - \bar{\gamma}_{\mathrm{D}} \tag{29}$$

Practically, we measure the mean decay rate of donor molecules at many different locations on the donor alone sample γ_D and the acceptor alone sample γ_{DA} which is discussed later. From these data we build up statistical uncertainties of our mean FRET strength that match with first principles theoretical predictions.

In the Ag and metamaterial samples, a 3.5 nm SiO_2 spacer layer is used to prevent complete fluorescence quenching at the metal surface. Due to slight instabilities in the ultrathin deposition of this SiO_2, the exact thickness of the cap layer varies from deposition to deposition (3.3-4 nm). From the quartz crystal monitor located inside the thin film deposition chamber, this variation is known for each run and this accounts for the variation in the exact magnitude of the effective decay rate for the donor and donor with acceptor samples. It is *important* to note that for a particular set of samples (e.g. donor alone and donor with acceptor for the "trilayer" metamaterial) the thickness of the spacer layer is fixed and the theoretical curves of the ensemble super-Coulombic FRET in the main paper has taken this into account.

1.1 Experimental Apparatus for acquiring Fluorescence Lifetimes

Figure S4 shows the schematic layout of the experimental setup to determine the fluorescent lifetime of the molecules in the experiment. We pump the samples from the *donor side* (reflection mode, figure S5) with $\approx 25-40$ fs, 400 nm laser pulses from an optical parametric amplifier (Spectra Physics NOPA 2H, 2016) which is in turn pumped by 1040 nm, 400 fs, 20 J laser pulses (Spectra Physics Spirit, 2016). The resulting fluorescence is collected by the same objective and sent through a variable filter wheel that can be used select different bands of emitted colors.

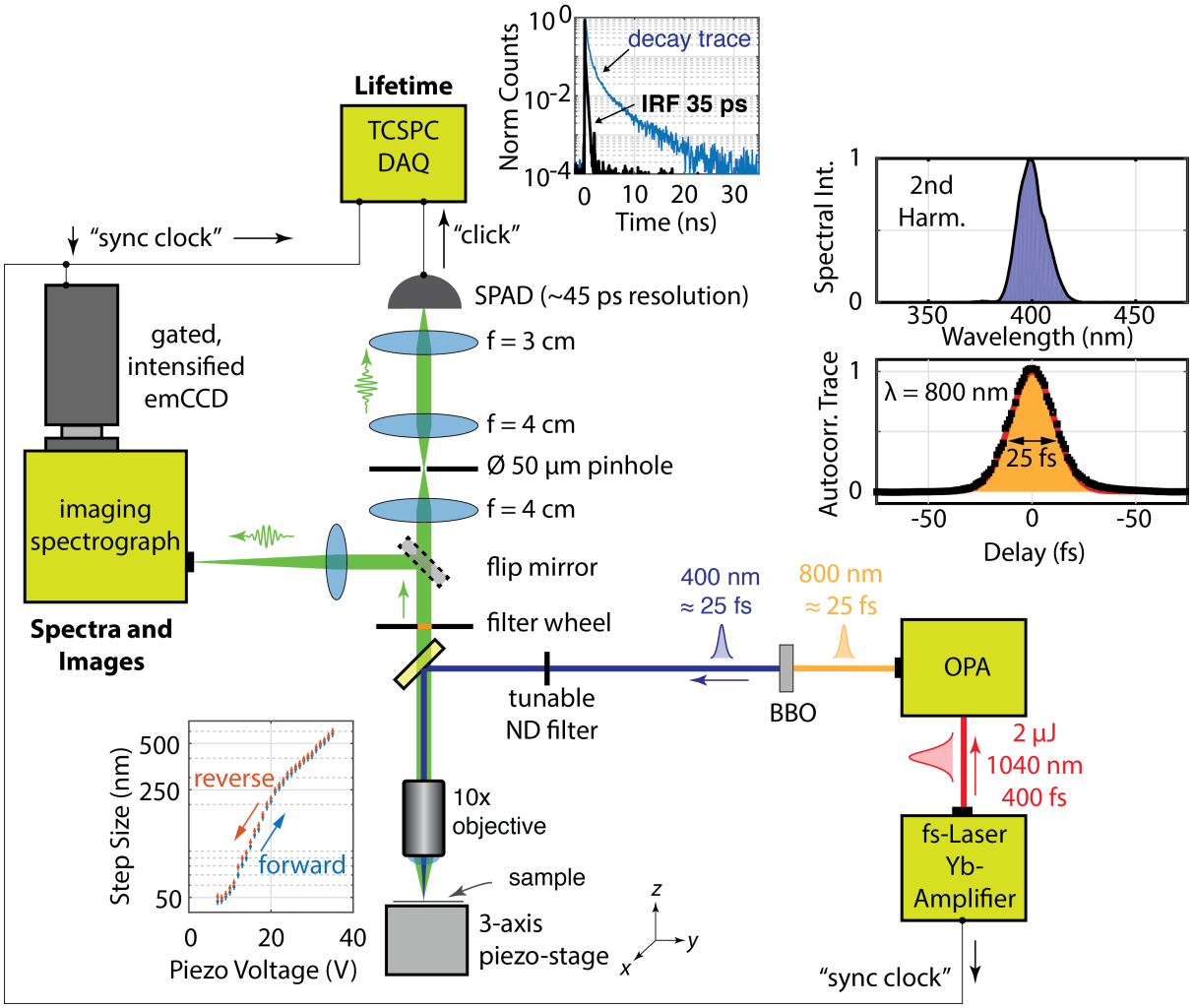

Fig. S4. Experimental apparatus for obtaining time-resolved fluorescence. The repetition rate of the pump laser is 100 KHz. The $\lambda = 400$ nm, 25 fs pulses arriving at the sample have pulse energies ranging from 0.01-100 nJ. Typical lifetime traces are acquired with pulse energies around 0.1 nJ.

The flip mirror allows us to divert the fluorescent emission to an imaging spectrometer to monitor the total spectrum of emission and the uniformity of the emission intensity. To monitor the emission spectra, we utilize a 450 nm long pass filter in the filter wheel and tune the spectrometer spectral dispersion window to $\lambda = 550$ nm. To directly image and ensure the uniformity of the emission intensity, we turn off the spectral dispersion of the spectrometer (tune the spectrometer grating so that the zeroth order, specular reflection is incident on the CCD) and open the entrance slit to the spectrometer. Different spectral color bands can then be imaged by selecting different narrow-band pass filters in the variable filter wheel. When the flip mirror is removed, the emission passes through a spatial filter and is then focused onto a single photon avalanche diode (SPAD) whose 'clicks' are referenced with the synchronized clock pulse of the pump laser. Statistics are then built up of the relative arrival times of the SPAD clicks (time correlated single photon counting, TCSPC). The approximate resolution (instrument response

function) of our SPAD/TCSPC system is $\approx$ 35 ps, measured with an extremely attenuated 500 nm, 100 fs pulse output from the OPA (see figure S4). Donor fluorescence emission is isolated from that of acceptor fluorescence and any background with a narrow band-pass filter centered on the blue edge of the donor PL spectrum. We use a three axis piezo electric translation stage, along with the imaging spectrograph to ensure we are acquiring lifetime data at a portion of the sample which has uniform fluorescence emission (no hot spots, scattering centers, nor areas of unusually bright emission). The calibration curve for the piezo electric translation stage is shown in figure S4.

The cross sectional area of the $\lambda = 400$ nm ultrafast optical excitation beam is $\approx 2\mu\text{m}^2$. For the same sample ($\approx$ 1"$\times$1" macroscopic size), individual data sets (10 or more points on a $\approx 10\mu\text{m}^2$ pitch square grid) are recorded at far separated areas of the sample (4 mm). These individual data sets are then averaged as shown in the fluorescence decay traces contained within the paper. The errors bars shown therein represent the uncertainty due to the spread in the measured individual decay traces. Note that the error bars contain (1) the shot noise of detection and, (2) the spread in measured data (standard deviation) due to long- (4 mm) and short-range (10 μm) non-ideal uniformities of sample geometry and dye concentration.

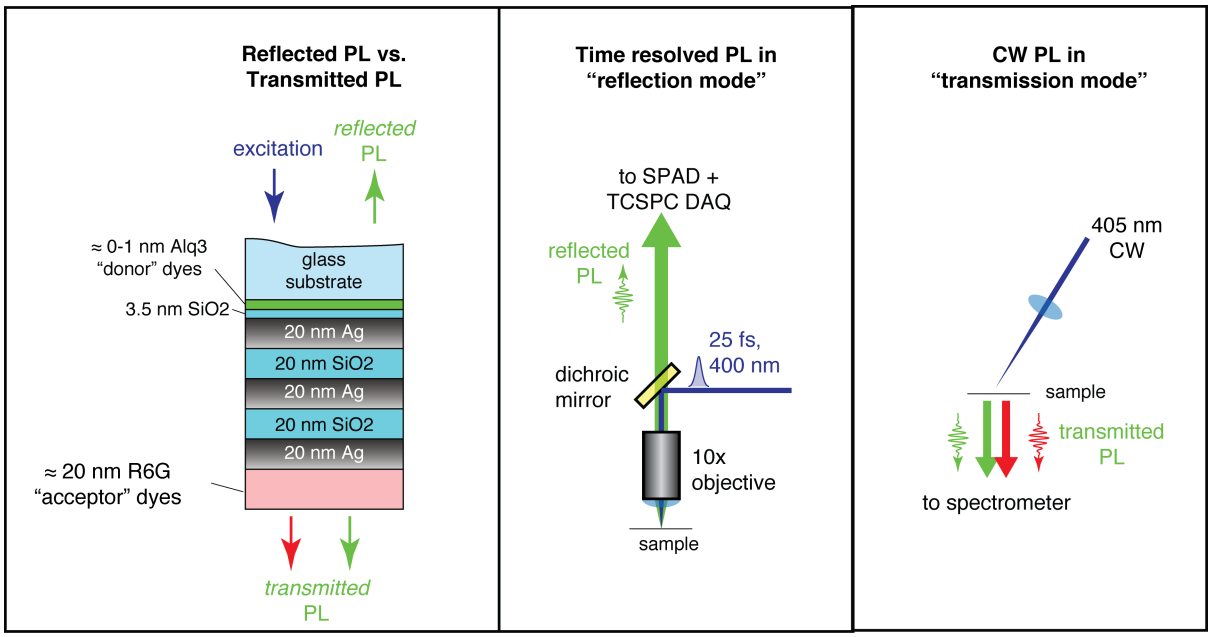

Fig. S5. Collecting fluorescence system and acceptor/donor plots. Reflected PL is used to monitor the donor fluorescence lifetime while the transmitted PL is used to monitor the acceptor fluorescent emission intensity. Both measurements are optically pumped with blue (pulsed or CW) from the donor-side of the sample, while they differ in which side the results fluorescence is collected from.

2 Steady State Energy Transfer Measurements

The experimental schematic is shown in figure S6. Steady state fluorescence measurements are taken in Transmittance mode as shown in figure S6 (a). This allows us to determine whether or not energy transfer (of any kind) is taking place across the samples. The samples are pumped from the donor side by about 24 μW of 405 nm CW laser (Spectra Physics Excelsior). The fluorescent emission (both donor and acceptor emission) is collected from the acceptor side (the opposite side of the thin films). The steady state spectra of the fluorescence is then measured with a fiber coupled high sensitivity CCD miniature spectrometer (made by Ocean Optics).

Control experiments were undertaken to test whether the background fluorescence emission of the undoped PMMA films and the nanofabricated Ag/SiO_2 multilayer metamaterial structure itself were present in the observed donor or acceptor spectra (Figure 3 in main manuscript). We find that the background spectra are at least one order of magnitude weaker than the transmitted Alq3 donor emission, and the R6G acceptor emission. The spectra shown in Figure 3 of the main manuscript are then reliable measurements of the Alq3 donor and R6G acceptor spectra.

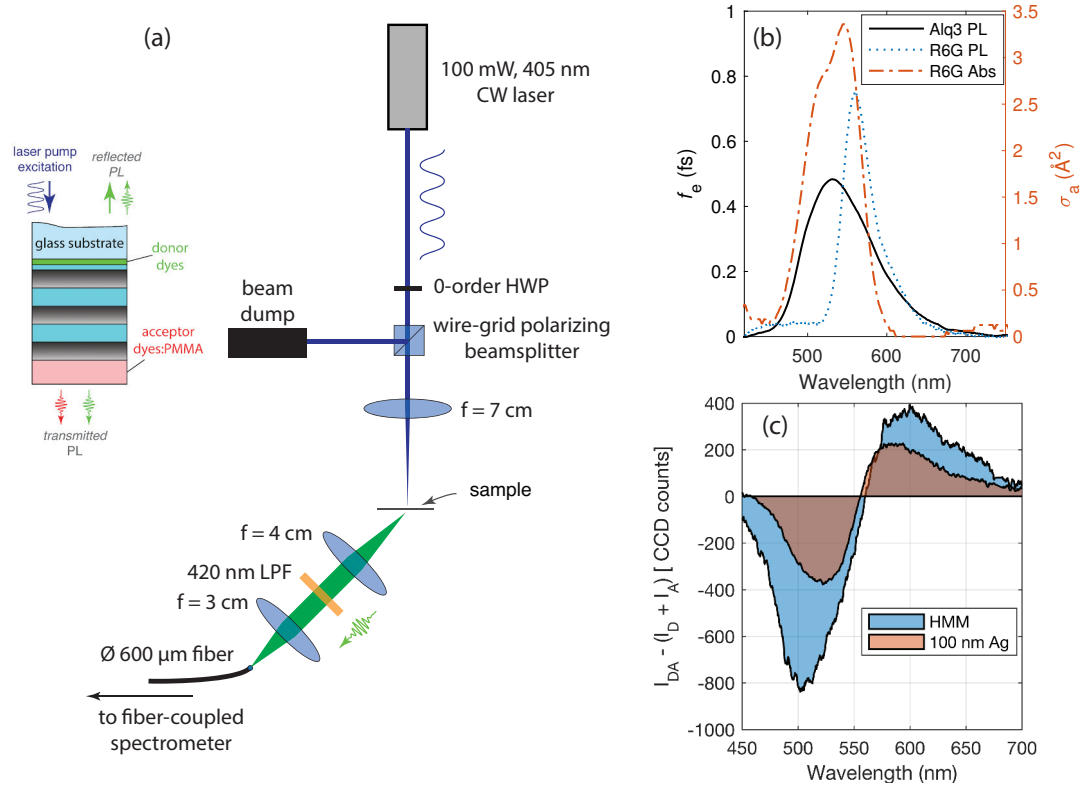

Fig. S6. Fabrication process flow for multilayer metamaterials displaying super-Coulombic interactions. (a) The experimental apparatus for measuring the steady state energy transfer *through* the dielectric, metal and metamaterial films. The transmitted steady state spectra, as defined in this figure, is recorded and shown in the main manuscript. (b) Photoluminescence emission and absorption cross section spectra of Alq3 and R6G dyes. Alq3 having a PL quantum efficiency of $\approx 35\%$ is spin-casted as a monolayer while R6G is spin-casted as 20 nm films in PMMA 495. From these curves, we estimate the FRET radius of the Alq3:R6G donor-acceptor pair to be $R_o = 5.1 \pm 0.1$. (c) Differential photoluminescence spectrum between the donor only, acceptor only and donor+acceptor hybrid samples where the two species of molecules are separated by 100 nm metamaterial or silver (control). The energy transfer is evident since the differential PL is negative near the donor spectrum (shorter wavelengths) and positive near the acceptor spectrum (longer wavelengths). The donor + acceptor hybrid samples are the only situation in which long-range dipole-dipole interactions can take place. Radiative energy transfer takes place in all samples but the lifetime change occurs only in the metamaterial sample indicative of long-range dipole-dipole interactions.

To help quantify the energy transfer across the metamaterial and silver films, we utilize the differential photoluminescence spectra. We subtract the summed emission spectra of the control samples (directly pumped donor alone and acceptor alone, $I_D + I_A$) from the emission spectra of the hybrid sample (donors with acceptors present across structure, I_{DA}). The differential spectra is then defined as $\Delta I = I_{DA} - (I_D + I_A)$. We see that the increase in acceptor emission ($\lambda \approx 570$ nm) due to FRET is always less in magnitude to the decrease in donor emission ($\lambda \approx 520$ nm) by a factor of approximately two. This is also a rough measure showing the energy transfer process is no where near 100% efficient.

3 Metamaterial Design and Forster Resonance Energy Transfer Pair Selection

Multilayer Metamaterial Design The hyperbolic medium is designed using a metal(Ag)-dielectric(SiO_2) plasmonic super-lattice with layer thicknesses (20 ± 2 nm), making the unit cell of the metamaterial much smaller than the central wavelength of donor emission at $\lambda = 525$ nm. This condition ensures the multilayer behaves like an effective medium. Using these equal SiO_2/Ag layers, of thicknesses 20 nm, allows a hyperbolic dispersion across the entire spectral overlap region between Alq3 donors and R6G acceptors. Deviations from effective medium theory are expected for high spatial frequency light, however, spectroscopic ellipsometry measurements confirm that the effective dielectric permittivity tensor of the multilayer can be approximated by $\epsilon_x \approx -4.2 + 0.2i$, $\epsilon_z \approx 5.4 + 0.01i$ at $\lambda = 525$ nm [21]. This confirms the type II hyperbolic metamaterial behavior essential to create Super-coulombic interaction pathways between donor and acceptor molecules, while simultaneously suppressing conventional radiative interactions as the propagating spatial modes in vacuum decay within the metamaterial (transmission $< 1\%$ at $\lambda = 525$ nm). In this multilayer metamaterial, the microscopic origin of super-Coulombic RDDI is the coupled charge oscillations of Bloch surface plasmon-polaritons supported by the thin silver films.

FRET Radius Estimation The FRET radius is the donor-acceptor distance at which the FRET rate will be equal to the spontaneous emission rate of the donor. It can be calculated from the following equation, derived from first principles [47]

$$R_o = \left[\frac{3c}{32\pi^4 n^4} \int_0^\infty f_D(\lambda)\sigma_A(\lambda)\lambda^2 \mathrm{d}\lambda \right]^{1/6} \tag{30}$$

Here c is the speed of light, n is the refractive medium of the donor-acceptor host medium, $f_D(\lambda)$ is the donor emission spectrum and $\sigma_A(\lambda)$ is the acceptor absorption cross section. The normalization imposed on $f_D(\lambda)$ is

$$\mathrm{QE} = 2\pi c \int_0^\infty f_D(\lambda)/\lambda^2 \mathrm{d}\lambda \tag{31}$$

where QE is the internal quantum efficiency of the Alq3, taken from literature to be around 0.35 [36]. Using the quantitative emission and absorption properties present in figure S6 (b), along with the quantum yield of Alq3 of ≈ 0.35, we find the FRET radius to be $R_o \approx 5.1 \pm 0.1$ nm.

4 Metamaterial Fabrication and Material Characterization

4.1 Fabrication

Silver and silica multilayer films were deposited on glass microscope slides using electron beam evaporation technique.

4.2 Determining Optical Constants

Optical constants of individual silica and silver films were determined using ellipsometry. The inferred optical constants showed good agreement with literature [37, 38]. We modeled the dielectric permittivity function of silver as $\epsilon_{Ag} \approx \epsilon_{FC} + \epsilon_{bound}$, with ϵ_{FC} being the contribution from the free carriers and ϵ_{bound} being the contribution of bound or valence electrons. Free electron motion in the silver is treated with a

Drude dispersion while interband transition of bound electrons in the UV are modeled with five Lorentz oscillators as described by Chen et al [34, 38]

$$\epsilon_{fc} \approx \epsilon_{drude} = 1 - \frac{\omega_p^2}{\omega^2 + i\omega/\tau} \tag{32}$$

$$\epsilon_{bound} \approx \epsilon_{bg} + \sum_{n=1}^{5} \epsilon_{lorentz} = \epsilon_{bg} + \sum_{n=1}^{5} \frac{A_n \omega_n^2}{\omega_n^2 - \omega^2 - i\omega/\tau_n} \tag{33}$$

ω_p is the plasma frequency of the metal, τ is the free electron scattering time, ω_n is the n^{th} interband transition frequency, τ_n is the dissipation time of the interband excitation, and A_n is the amplitude of the interband excitation. ϵ_{bg} represents a background dielectric constant from the metal's core-shell electrons.

The effective dielectric tensor used in the effective medium theory was extracted for the five-layer Ag/SiO_2 sample using spectroscopic ellipsometry. The ϵ_x component was modeled using a modified Drude dispersion whereas the ϵ_z component was modeled with a Lorentz oscillator. Discussion and analysis of the effective medium theory used here is extensively discussed in literature [21, 22, 39, 40,41, 42, 43].

4.3 Fluorescent Dye Film Fabrication

Donor, Alq3 films Alq3 molecules dissolved in Chloroform are spin-coated to create $\leq$ 1 nm thin films. A few drops of 5mg of Alq3 in 15 ml chloroform are spun on a substrate at 8000 RPM for 60 s. The high volatillity of chlorofom and the spin speed ensure that only a uniform thin film of Alq3 dye molecules remain on the substrate.

Acceptor, R6G:PMMA films R6G and PMMA are dissolved in a solution of anisole and methanol. Our R6G:PMMA thin films are made in a similar manner as the Alq3 thin films. These films are annealed at 180 ^{o}C, a temperature higher than the boiling temperature of the solvents. This ensures no solvents reamin and also reflow the PMMA film. Pre-anneal and post-anneal measurements of the R6G:PMMA fluorescence emission intensity confirm that the annealing process does not degrade or significantly alter the emission profile of the R6G dyes.

4.4 Determination of dye film thicknesses and the dye concentrations

Acceptor, PMMA:R6G films In order to determine the thickness and optical wavelength scale uniformity of the R6G:PMMA films using ellipsometry , we first refine the dielectric permittivity function for undoped PMMA films. A Cauchy model with a UV absorption band edge is utilized for PMMA, where local thickness measurements yield a ± 0.5 nm uncertainty. The variation of PMMA thickness across the entire sample leads to a thickness uncertainty of ± 1.5 nm.

We then spin-cast R6G doped PMMA films, as described above. Using ellipsometry, we determine the thickness of this film utilizing the undoped PMMA model, fitting the spectroscopic ellipsometry data for wavelengths longer than the absorption band of the R6G ($\lambda > 600$ nm). For our R6G:PMMA solutions, we estimate our final acceptor R6G:PMMA films to have a thickness of 20 ± 1.5 nm.

To determine the R6G dye concentration in the vicinity of the metamaterial, we ulilize thin-films of R6G:PMMA spin-casted on glass substrates where we model the transmittance T through a film with the Beer-Lambert law

$$-\log_{10} T = \sigma \int \mathrm{d}z \; c(z) \tag{34}$$

where σ is the absorption cross section of the dye and $c(z)$ is the dye concentration profile of the film (remember the films are uniform in thickness to $\pm 7\%$, so there is a translation invariance in the xy-plane). In this case the transmittance is $T = P/P_o$, where P is the power transmitted through the glass substrate and the thin film of R6G:PMMA, while P_o is the power transmitted through an equal thickness film of undoped PMMA on glass. We assume that the concentration profile is uniform within the film so that the dye concentration is c within the film and zero elsewhere. It then follows that the dye concentration can be estimated from the relation

$$c = \frac{-\log T}{L\sigma} \tag{35}$$

where L is the film thickness. The absorption cross section of R6G in PMMA is approximately 3.36 $\mathring{A}^2$, the film thickness is $L = 20 \pm 1.5$ nm, and the negative logarithm of the transmittance is measured to be as $\log T = 0.05 \pm 0.01$. We then estimate the acceptor R6G concentration in the vicinity of the metamaterial as

$$C = 0.074 \pm 0.012 \text{ particles } /\text{nm}^3 = 7.4 \times 10^{21} \pm 1.2 \times 10^{21} \text{ particles } /\text{cm}^3 \tag{36}$$

These calculations agree closely with the Stoichiometric calculation of $c = 0.070 \pm 0.05$ particles $/\text{nm}^3$, based on the initial molar concentrations of the R6G dye and PMMA in the initial spin-casting solution.

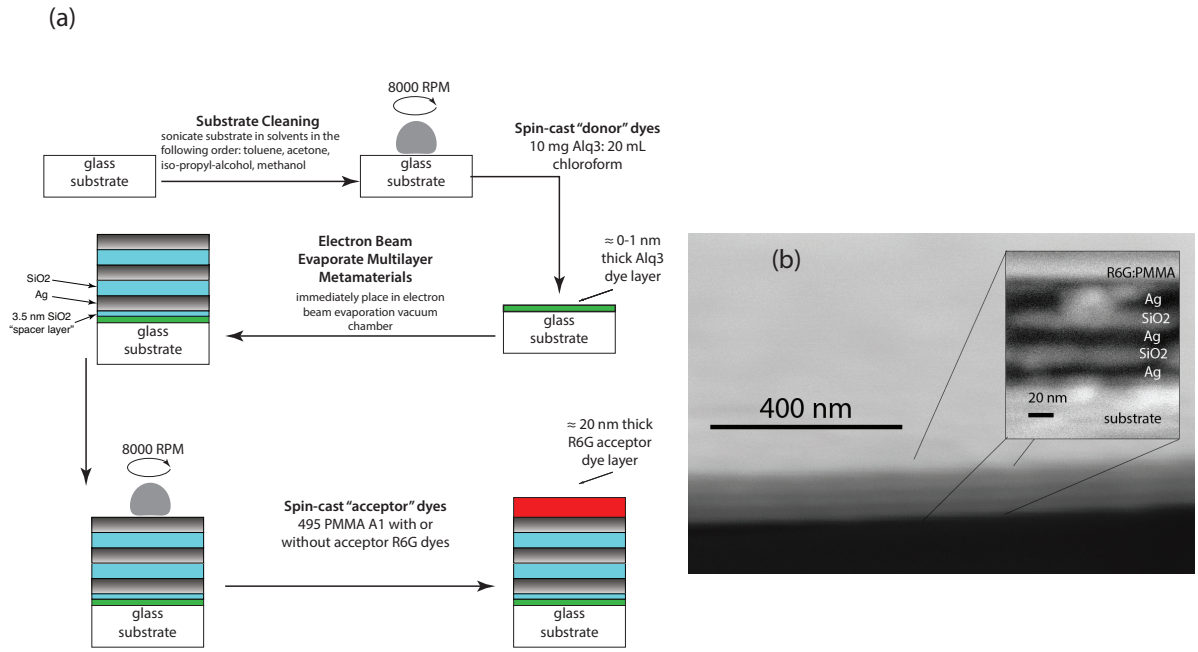

Fig. S7. Background fluorescence. (a) Fabrication process flow for multilayer metamaterials displaying super-Coulombic interactions. Metal dielectric films are fabricated using electron beam evaporation. Donors are deposited as thin as possible by choosing the volatile solvent chloroform (with no dissolved PMMA) as the spin-solution. R6G Acceptor films are deposited via spin-casting in a PMMA matrix. We deposit a 3.5 nm SiO_2 *spacer*-layer to prevent complete quenching of the Alq3, donor fluorescence by the first metal interface. Individual Ag and SiO_2 layer thicknesses are chosen to be 20 nm leading to a broadband hyperbolic dispersion for the multilayer stack for $\lambda > 370$ nm. (b) SEM micrograph of the nanofabricated HMM structure is shown.

5 Uncertainty and Noise in Experiment

In this section we discuss two main sources of uncertainty in our experiments: (1) fluctuating background noise and fluorescence and (2) systematic uncertainty due to nanofabrication imperfections.

5.1 Background fluorescence emission

Thin films of SiO_2 and PMMA both fluoresce in the green part of the visible at ns-time scales under UV light excitation. Since our pump is an ultrashort pulse centered around 400 nm (see figure S4), we must ensure that any emission from the Ag/SiO_2 metamaterial structure itself, as well as any emission from undoped PMMA film, do not cloud our measurements on the donor emission kinetics. Figure S8 shows (1) the background fluorescence emission that is present in our donor measurements of the metamaterial sample and, (2) the signal intensity for the donor only sample. We find that at the fluorescence peak of Alq3 ($\lambda \approx 520$ nm), the total time integrated background flourescence is approximately 250x weaker than the total time integrated Alq3 emission.

the time dynamics of background emission from the metamaterial structure at a wavelength of $\lambda = 500$ nm were measured. This background emission displays two distinct time scales. Over 75% of the emission decays in the first 500 ps after the ultrafast laser excitation, while the remaining fluorescence slowly decays at a time scale of ≈ 200 ns. The background fluorescence emission can alter our donor emission kinetics, which we discuss here in breif.

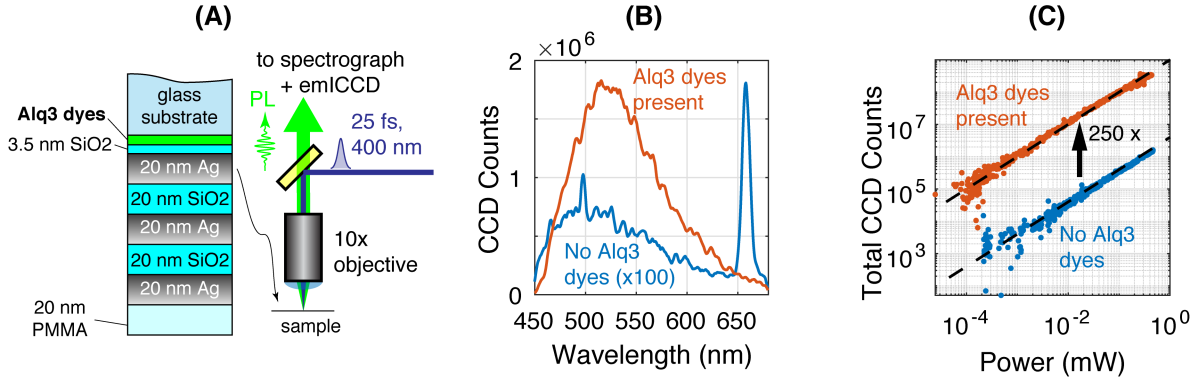

Fig. S8. Donor life time measurements. (A) We pump the metamaterial structure with ultrashort 25 fs laser pulses centered at $\lambda = 400$ nm from the substrate, donor-side side of the sample. The resulting fluorescence is collected in a confocal geometry with a 10x objective and sent to a spectrograph coupled with a high sensitivity gated CCD. (B) The metamaterial control sample with no Alq3 donor dyes present (note: the undoped PMMA film is still present) shows a broad fluorescence in the green and a sharp fluorescent peak around $\lambda = 660$ nm. This sharp fluorescence peak in the background signal is well out of the range of detection of our emission time dynamics measurements which are centered at $\lambda = 500$ nm. (C) Fluorescence intensity versus incident laser pump power is shown for the control sample (no dyes present) and the Alq3-doped (donor alone) metamaterial sample. We find that both fluorescence signals are in the linear regime (dashed lines are linearly proportional to pump power) at our experimental bandwidth of $\lambda = 500$ 20 nm. Furthermore, at all pump powers the background fluorescence (blue) is about 1/250x the intensity of the Alq3-doped metamaterial (red).

The time resolved fluorescence lifetime measurements presented in the manuscript are performed via time-correlated-single-photon-counting at a fixed count rate (i.e. signal level reaching the single photon detector), not at a fixed excitation pump power. Each raw trace then has approximately a constant number of total counts (i.e. fixed area). This is in contrast to the CW steady state spectra measurements; these spectra were taken at fixed pump power so that the absolute signal magnitudes reveal evidence of energy transfer. However, in the time resolved emission, the true evidence of near-field-like energy transfer is in the reduction of the excited state lifetime, not entirely in the absolute magnitude of the decay traces. We have chosen to normalize our traces to 1 to make visually clear the reduction in the excited state lifetime of the donor as well as to determine the average FRET rate (see Section B1 above).

The donor emission intensity is quenched when acceptors are present on the other side of the metamaterial and we thus increase the 400 nm laser pump intensity such that the donor emission signal level reaching our detectors remains at a fixed 1000 counts per second, corresponding to approximately 1% of our laser repetition rate. In the hybrid (donor with acceptor) sample, we typically have to increase our pump intensity no more than two times the pump intensity of the donor alone sample. Since the background and donor fluorescence emission is in the linear regime (see figure S8(C)), we can expect that our background fluorescence emission in the hybrid sample can contribute twice as much as in the donor alone sample. We now show this increase in background fluorescence can not account for our decrease in donor lifetime in the hybrid sample.

5.2 Noise due to Nanofabication Inperfections

AFM measurements have shown that the Alq3 donor and SiO_2 capping layer vary in total nominal thickness in the order of 1-2 nm at distance scales of 10's of μm. In our optical setup, the objective focuses the 400 nm pump laser to a spot sixe of $\approx$2 μm. The donor fluorescence emerges from this region. Therefore a single measurement samples a population of dyes with a different near-field environment than other locations on the substrate. The donor LDOS and donor-acceptor FRET is very sensitive to the dye's proximity to the interface, this causes different emission kinetics in consecutive measurements at unique locations on the substrate. Specifically, the long-time emission kinetics are dominated by the donors that are farthest from the metamaterial/PMMA interface.

In the results presented in the main manuscript, we sum 10 decay traces from different locations on the substrate. The representative decay traces for donor alone and donor with acceptor samples are shown in figure S9. The error bars shown in the decay traces in the main manuscript represent the uncertainty (standard deviation in the spread of measurements) due to (1) shot noise and (2) the variation in emission kinetics from nanofabrication imperfections.

In the figure S9 we show the un-normalized decay traces for the case of a donor film separated by the 100 nm HMM from a 20 nm PMMA film (donor alone I_D) and the case of a donor film separated by the 100 nm HMM from a 20 nm thick acceptor doped PMMA film (donor with acceptor I_{DA}). We plot the difference between these two fluorescence decay trace signals shown in figure S9 (c).

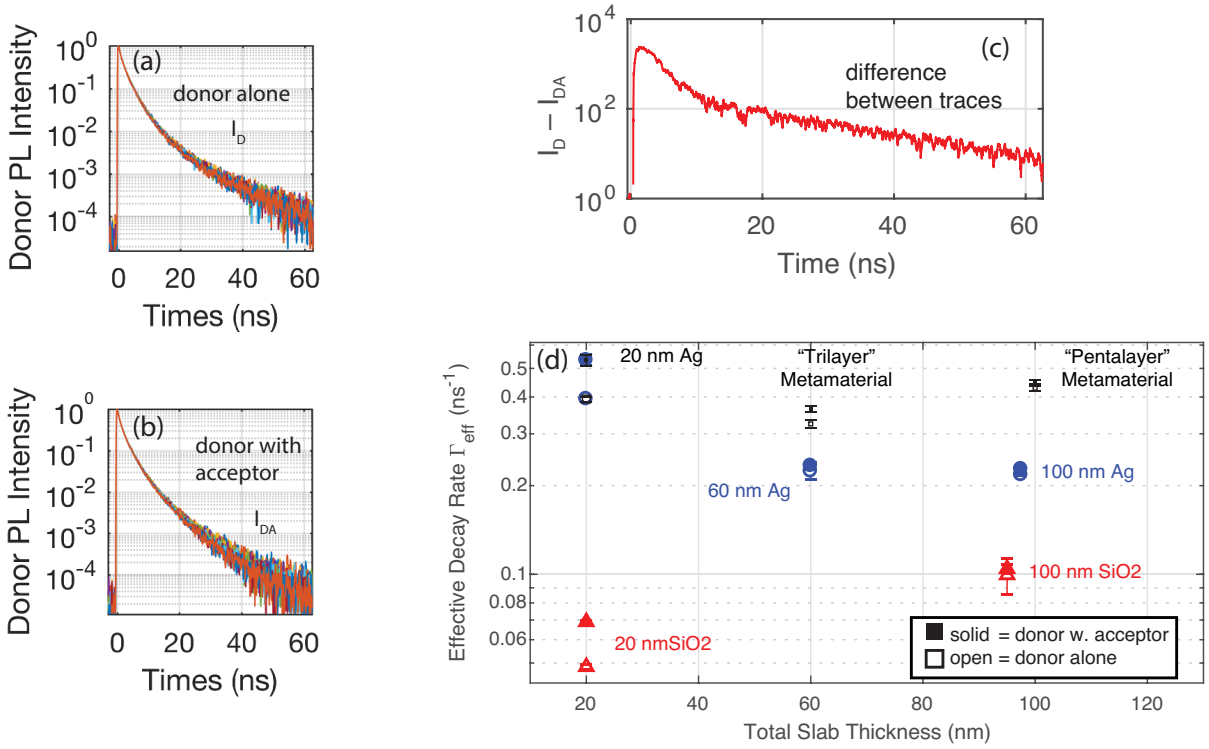

Fig. S9. Raw donor lifetime traces and extracted measurements. Figure: (top) The decay traces for the donor only and donor+acceptor hybrid sample separated by the 100 nm metamaterial. (bottom) The difference in decay traces showing clear evidence of the super-Coulombic interaction since the number of counts in any bin is well above the noise floor.